Numerical treatment of boundary conditions to reduce high-frequency artifacts in simulations of distributed-feedback lasers

T.I. Lakoba, B.L. Kotzen, and C.J. McKinstrie

Abstract—**High-frequency artifacts may occur when the coupled-mode equations describing distributed-feedback lasers are solved by a variety of numerical methods, such as method-of-characteristics schemes and the split-step method. We propose a simple technique to suppress this artifact. Its idea is to modify the numerical implementation of the boundary conditions to promote the leakage of highest-frequency modes out of the medium. At the same time, this implementation only minimally affects the physical part of the solution. We demonstrate the effectiveness of this technique for first- and second-order schemes.**

Index Terms—**Distributed feedback devices, Semiconductor device modeling**

I. INTRODUCTION

Semiconductor distributed-feedback (DFB) lasers are the backbone of the optical communications industry and also find extensive applications in compact optical sensing devices. Their operation involves stimulated and spontaneous emission, stimulated absorption, material and facet loss, and the coupling of forward and backward light waves. In the lasing regime, the dynamics of these waves results in longitudinal and/or transverse mode competition. A good laser will attain a single-mode steady state, superimposed on which are weak, noise-induced power and frequency fluctuations. The light-wave and carrier-electron equations that govern laser dynamics are too complicated to solve analytically. Consequently, one must use numerical simulations to determine the properties of a variety of designs. To do this, one must have a code that operates accurately and stably, even in the presence of noise. In this work we address the issue of suppression of an artifact, which may appear as a numerical instability, in some widely used numerical schemes. Surprisingly, this artifact has not, to our knowledge, been discussed in the earlier literature on numerical modeling of DFB devices.

Electromagnetic wave propagation in semiconductor lasers with distributed feedback is modeled by the following equations for forward- and backward-propagating fields $E^\pm$ and free carrier (electron) density N (see, e.g., [1], [2], [3]):

$$\left(\frac{1}{v_g}\partial_t \pm \partial_x\right) E^\pm = f^{(\pm)}(E^+, E^-, N) + \xi^\pm(x, t),\quad \text{(1a)}$$

$$\partial_t N = f^{(N)}(E^+, E^-, N) - v_g \left((E^+)^* \xi^+ + (E^-)^* \xi^- + \text{c.c.}\right).\quad \text{(1b)}$$

T.I. Lakoba and B.L. Kotzen are with the Department of Mathematics and Statistics, University of Vermont, Burlington, VT 05405, USA; e-mail: tlakoba@uvm.edu

C.J. McKinstrie is at 3 Red Fox Run, Manalapan, NJ 07726, USA

Here t and x are the time and distance along the propagation direction; v_g is the field's group velocity; $\xi^\pm$ are mutually independent noise terms modeling spontaneous emission; the asterisk denotes complex conjugation, and 'c.c.' stands for 'complex conjugate'. The functions on the r.h.s. in (1) are:

$$f^{(\pm)} = \left(\frac{g\left(1 + i\Delta\right)\left(N - N_0\right)}{2(1 + \varepsilon P)} - \frac{\alpha_{\text{loss}}}{2}\right) E^\pm + i\kappa E^\mp,\quad \text{(2a)}$$

$$f^{(N)} = \frac{J}{qd} - \frac{N}{\tau} - BN^2 - CN^3 - \frac{g\left(N - N_0\right)}{1 + \varepsilon P} v_g P,\quad \text{(2b)}$$

where g is the differential gain (including the confinement factor), Δ is the linewidth enhancement factor, N_0 is the carrier density required for transparency, $P = |E^+|^2 + |E^-|^2$ is the total photon power (normalized so that it has units of density N, i.e., that of inverse volume), ε is the gain compression coefficient, α_{loss} is the waveguide loss coefficient, and κ is the coupling coefficient due to refractive index corrugation (we do not consider gain coupling in this work, as it is not essential to its main idea). Moreover, in (2b), J is the current injection density, q is electron's charge, d is the thickness of the active layer, τ is the carrier lifetime, B and C are bimolecular and Auger recombination coefficients, respectively. The spontaneous emission terms are assumed to have the correlation functions:

$$\langle(\xi^\pm)^*(x', t')\,\xi^\pm(x, t)\rangle = 2D_\xi^\pm \delta(x - x')\,\delta(t - t'),\quad \text{(3)}$$

where $\langle\cdots\rangle$ stands for ensemble average, and all the other correlation functions vanish. Strictly speaking, Eq. (1b) also has a noise term whose intensity is proportional to the carrier recombination rate [1]. For the parameters that we consider below, that intensity is of the same order of magnitude as that of the noise term retained in (1b). As we show in Section 4, the effect of that noise term is quite small (much smaller than the effect of the noise terms in Eqs. (1a)), and hence we limit ourselves to considering only one type of noise term in (1b).

The partially reflecting boundary conditions (BC), which along with Eqs. (1)–(2) govern the lasing dynamics of the device, are:

$$E^+(+0, t) = T_l E_{\text{inc}}^+(t) + R_l E^-(+0, t),\quad \text{(4a)}$$

$$E^-(L - 0, t) = T_r E_{\text{inc}}^-(t) + R_r E^+(L - 0, t),\quad \text{(4b)}$$

where $T_{l,r}$ and $R_{l,r}$ are, respectively, the complex transmission and reflection coefficients at the left ($x = 0$) and right ($x = L$) boundaries, and $E_{\text{inc}}^\pm(t)$ are the forward- and

backward-propagating fields incident on the device from the outside. The fields at the output of the device are found from:

$$E^-(-0,t) = T_l^* E^-(+0,t) - R_l^* E_{\mathrm{inc}}^+(t), \tag{5a}$$

$$E^+(L+0,t) = T_r^* E^+(L-0,t) - R_r^* E_{\mathrm{inc}}^-(t). \tag{5b}$$

We will consider lasing as starting from spontaneous emission, described by the initial condition

$$E^\pm(x,0) = \zeta^\pm(x), \qquad N = N_0, \tag{6a}$$

where $\zeta^\pm$ is a white noise in x similar to that defined in (3):

$$\langle (\zeta^\pm)^*(x')\, \zeta^\pm(x) \rangle = 2D_\zeta^\pm \delta(x-x'), \quad \text{etc.} \tag{6b}$$

We will work with nondimensionalized equations, letting

$$x \to xL, \quad t \to t\,(L/v_g), \quad N \to N\,N_0, \quad P \to P\,N_0; \tag{7a}$$

here, on the left (right) the variables x, t, N, P are dimensional (nondimensional). Equations (1), (2) written in these nondmensional variables retain their form, where now all the coefficients are appropriately normalized and, in addition:

$$0 \le x \le 1 \text{ (i.e., } L=1); \quad v_g = 1; \quad N_0 = 1. \tag{7b}$$

Most numerical methods used to solve the coupled-mode Eqs. (1) fall into two categories: transfer matrix-type methods and finite-difference schemes based on the Method of Characteristics (MoC). These two categories were compared in [4], [5]. In Appendix A we will also briefly describe two forms of the split-step method. In this work we focus on the schemes based on the MoC [6], [2], [7]; however, the ideas developed below apply equally to the split-step method. In [6], [2], the MoC schemes were referred to as 'transmission line laser model' and 'time domain model,' respectively; they produced first-order accurate (in time step) solutions of Eqs. (1). In Ref. [7], a fourth-order scheme was used; other fourth-order MoC schemes are found in [8], [9], although they were not used specifically to solve Eqs. (1). Below we focus on a second-order MoC scheme, described in Appendix A, where we also justify our choice of this order of accuracy. Let us note that among various finite-difference methods, MoC schemes present a "natural choice" in that the numerical grid can be chosen so that characteristics of the system cross exactly at the grid nodes.

The numerical difficulty faced by the MoC applied to Eqs. (1), (2), and (4) can be illustrated with the following example. The stationary ($\partial_t \equiv 0$) solution of these equations with normalization (7), nondimensional parameters (see caption to Fig. 1):

$$\Delta = \epsilon = \alpha_{\mathrm{loss}} = 0, \quad g = 10, \quad \kappa = 2,$$
$$\frac{1}{\tau} = 10^{-3}, \; B = \frac{0.6}{\tau}, \; C = \frac{0.9}{\tau}, \; \frac{J}{qd} = \frac{25}{\tau}; \tag{8a}$$

$$E_{\mathrm{inc}}^\pm \equiv 0, \quad R_r = 0, \quad R_l = -i\sqrt{0.9}, \tag{8b}$$

and $\xi^\pm \equiv 0$, is shown in Fig. 1(a). This solution can be obtained, e.g., with the shooting method. On the other hand, the solution at $t \gg 1$ obtained by the MoC scheme of

Appendix A is shown in Fig. 1(b). The output power at the left boundary is shown in Fig. 1(c). Both figures show numerical artifacts occurring due to significant presence in the solution of the mode with the highest numerically resolved frequency. In Fig. 1(b) and the inset to Fig. 1(c), this is manifested by the curve's changing significantly on the scale of the grid spacing h. This numerical artifact persists as h decreases (we verified this down to $h = 1/2000$), although its magnitude relative to the smooth part of the solution varies irregularly with h. This persistence of the artifact for progressively smaller grid spacings indicates that it is a purely numerical phenomenon and is *not* related to the physical high-frequency pulsations due to mode competition, reported, e.g., in Fig. 6 of [2].

Figure 1(d) confirms that the highest resolved (i.e., unphysical) Fourier harmonics are not sufficiently attenuated by the numerical scheme compared to the harmonics with wavenumbers $O(1)$ (i.e., those describing the actual physical process). It should be noted that the shape of the Fourier spectrum (and, most importantly, the relative magnitude of the highest and lowest harmonics) remains approximately the same even for much longer times than that used in Fig. 1; e.g., for 1000 nondimensional units, or about 5 ns. In other words, the highest-frequency harmonics do not grow in time, but are merely not attenuated fast enough compared to the "physical" part of the solution. Thus, the artifact described above is *not a numerical instability* (in the terminology of numerical analysis). Rather, it is an unphysically slow decay of the highest harmonics resolved by the numerical grid compared to the time evolution of the lower-frequency modes that describe the "true" physics of the model. Those "physical" modes occupy part of the Fourier spectrum with wavenumbers of order one, as follows from the coefficients in the example considered, i.e., (8), all being of that order. Even for $h = 1/100$, used in Fig, 1, and certainly for the smaller grid spacings mentioned above, the "physical" modes are very well resolved by the numerical grid.

We have explained that the highest-frequency modes are present in the solution because the numerical scheme causes them to decay insufficiently fast. To see how these modes became part of the solution, recall that in the simulations reported in Fig. 1, lasing is assumed to be seeded by the spontaneous emission (6). There, harmonics with all wavenumbers contribute approximately equally. According to Fig. 1(d) and to the analysis presented later in this paper, the magnitude of the lowest and highest harmonics evolves at approximately the same rate, while the intermediate harmonics decay faster. Then, it is the smooth and the most rapidly varying harmonics that dominate the numerical solution at long times. If, on the other hand, the field inside the medium is excited, e.g., by an incident pulse, then the situation can be different; see below.

Let us note that, to our knowledge, the high-frequency numerical artifact illustrated in Fig. 1 was *not* reported in earlier studies. We do not know why this was the case. In regards to studies (e.g., [2], [4], [10]) which considered lasing, that presumably was seeded by spontaneous emission, we hypothesize that the authors could have started their simulations with spatially smooth, small but nonzero initial values of $E^\pm$ inside the medium. If these smooth initial values significantly
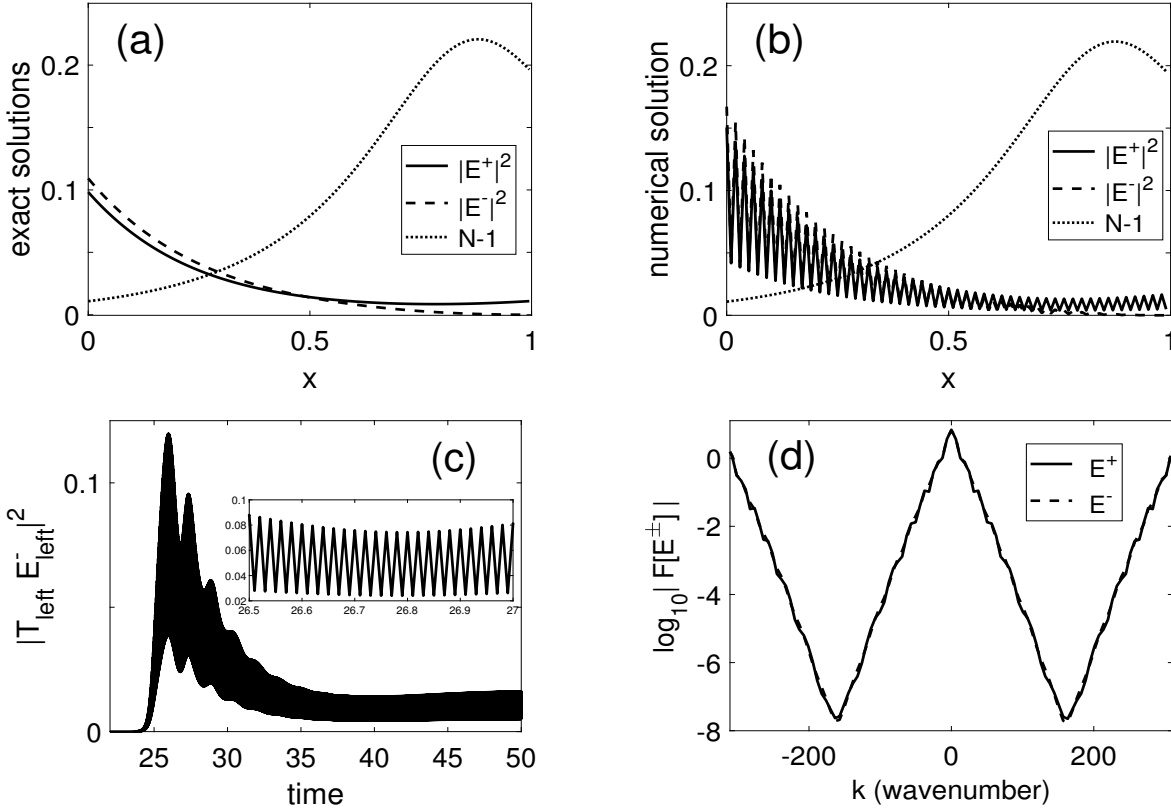
Fig. 1. (a): Stationary solution of Eqs. (1)–(4) where $\xi^{\pm} \equiv 0$, and (8); all variables are nondimensionalized as per (7). One nondimensional time unit corresponds to ~ 5 ps. (b): Solution of the same system with $D_{\zeta}^{\pm} \sim 10^{-30}$ (i.e., the order of Matlab's round-off error) in (6b) obtained by the MoC scheme described in Appendix A at $t = 100$ with $h = 0.01$. (c): A sample of output power evolution at the left boundary. (d): Fourier spectrum of the forward- and backward-moving fields at $t = 100$. In (c), the graph appears as a filled band due to fast unphysical oscillations at the maximum frequency resolved by the temporal grid; a close-up on these oscillations near $t = 27$ is shown in the inset, confirming that they occur at the highest resolved frequency with period h. For (d), the fields were multiplied by a super-Gaussian window to ensure periodicity in x before taking the Fourier transform. Parameters (8) represent a version of parameters used in Section 4 that was simplified ($\Delta\omega = \epsilon = \alpha_{\text{loss}} = 0$) but retain the most essential features of the model, e.g., the relaxation oscillations seen for $25 < t < 30$. Some other parameters were tweaked so that in the absence of the high-frequency numerical artifact, the lasing would occur at a single frequency. See Section 4 for more details.

exceeded the level of (initial) spontaneous emission, so would the amplitude of smooth, physical modes compared to those of the highest-frequency, unphysical modes. As we noted in the previous paragraph, this relation would then be preserved in time by the numerical scheme, and the fast ripple would not contaminate the numerical solution. We verified that this "trick" can indeed suppress the artifact. On the other hand, Ref. [7], which focused on transmission and and reflection of a smooth pulse through/from a grating containing an active medium. In this case, it appears likely that the field of that pulse could play the role of the "regularizing" smooth initial condition mentioned a few sentences ago, which thereby also suppressed the high-frequency artifact.

Let us note that the numerical artifact in question does *not* require the coupled-mode equations to have the complexity of all terms in Eqs. (1), (2). Rather, it is readily observed (when starting from zero, to numerical precision, initial conditions) even in the simplest coupled-mode system, as described in Section 2. Moreover, in Section 5 we show that the same artifact is observed (and can be suppressed with the technique presented in this work) in a split-step numerical method.

In this work we describe how the implementation of the BC (4) can be modified *in a systematic way* so that the high

Fourier harmonics "responsible" for the above artifact get attenuated sufficiently fast, similarly to what would be required by the physics of the problem (see the figures in Appendix B). Our modification of the BC restores the smooth nature of the solution obtained without the (physical) noise terms in Eqs. (1a) and produces a significantly smoothed solution when those terms are included.

The main part of this paper is organized as follows. In Section 2 we present the main idea of our smoothing method for the first-order MoC scheme and simpler equations. These simplifications are intended to clarify the presentation, allowing us to emphasize the idea over technical details. We also validate this idea numerically. In Appendices B and C we present analyses of the numerical method whose results corroborate our numerical results for the simpler case mentioned above. In Section 3 we extend the "smoothing" idea to a second-order MoC scheme and confirm its viability with numerical results, still for the simpler equations. Finally, in Section 4, we apply "smoothing" to simulate the original Eqs. (1)–(4), which include the noise terms, with the second-order MoC scheme of Appendix A, thus demonstrating the validity of the proposed method. In Section 5 we summarize the results and present some extensions.

II. SMOOTHING METHOD FOR A SIMPLIFIED PROBLEM

A. *Idea of the method*

To emphasize the key idea, we explain it here for a version of the original problem where we make two simplifications. First, instead of Eqs. (1), (2), we consider a system

$$(\partial_t \pm \partial_x)\, E^\pm = i\kappa E^\mp \qquad (9)$$

supplemented with the same BC (4), where we set $E^\pm_{\text{inc}} \equiv 0$. The phenomenon where the lowest and highest Fourier harmonics evolve at similar rates, thus causing numerical artifacts illustrated in Figs. 1(b,c), takes place for this simplified model as well. Second, in this section only, we will consider not the second-, but the first-order MoC scheme given by Eqs. (32), (34). Applied to Eqs. (9), this scheme reads:

$$\left(\begin{array}{c} E^+ \\ E^- \end{array}\right)^{n+1}_m = \mathcal{C}^+ \left(\begin{array}{c} E^+ \\ E^- \end{array}\right)^n_{m-1} + \mathcal{C}^- \left(\begin{array}{c} E^+ \\ E^- \end{array}\right)^n_{m+1}, \qquad (10a)$$

where: $(E^\pm)^n_m \equiv E^\pm(x_m, t_n)$ are field values at the nodes of the space–time grid; the evolution matrices for the forward- and backward-propagating fields are:

$$\mathcal{C}^+ = \left(\begin{array}{cc} 1 & 0 \\ 0 & 0 \end{array}\right) + h \left(\begin{array}{cc} 0 & i\kappa \\ 0 & 0 \end{array}\right), \quad \mathcal{C}^- = \left(\begin{array}{cc} 0 & 0 \\ 0 & 1 \end{array}\right) + h \left(\begin{array}{cc} 0 & 0 \\ i\kappa & 0 \end{array}\right); \qquad (10b)$$

and h is the step size in space and time. The standard implementation of BC (4) (with $E^\pm_{\text{inc}} \equiv 0$) is:

$$\left(E^+\right)^n_0 = R_l \left(E^-\right)^n_0; \qquad \left(E^-\right)^n_M = R_r \left(E^+\right)^n_M. \qquad (11)$$

Analysis of numerical scheme (10), (11) proceeds by using the ansatz

$$\mathbf{E}^n_m = \lambda^n \rho^m \mathbf{u}, \qquad (12)$$

where $\mathbf{E} \equiv [E^+; E^-]^T$ and vector $\mathbf{u}$ is independent of (m, n). The so-called amplification factor $|\lambda|$ and the parameter ρ determine, respectively, the temporal evolution and spatial shape of modes of the numerical scheme, which are non-periodic counterparts of Fourier harmonics. In particular, counterparts of Fourier harmonics with low ($|k| = O(1)$) and highest ($|k| \lesssim k_{\max} \equiv \pi/h$) wavenumbers k, are modes that correspond to physical (i.e., "true") and unphysical parts of the numerical solution and thus are referred to by these names in what follows. Separate analyses for these modes are presented in Appendices B and C. In particular, they show that:

- The physical and unphysical modes have:

$$\rho_{\text{ph}} = 1 + O(h), \qquad \rho_{\text{unph}} = -1 + O(h) \qquad (13a)$$

(note that $\rho_{\text{ph}} \approx \exp[i \cdot O(1) \cdot h]$ and $\rho_{\text{unph}} \approx \exp[i \cdot (\pi/h) \cdot h]$). Indeed, the physical modes are assumed to be numerically well resolved, meaning that they vary smoothly from one grid point to the next. The above factor $(\rho_{\text{ph}})^m$ describes such a smooth variation. On the contrary, the highest-frequency modes are not well resolved, meaning that they have only two grid points per period (as per the Nyquist criterion), at the maximum and minimum. The corresponding abrupt changes in the mode's profile are described by the factor $(\rho_{\text{unph}})^m$ and are illustrated, e.g., in the inset to Fig. 1(c).

- The corresponding amplification factors are approximately the same:

$$|\lambda_{\text{ph}}| \approx |\lambda_{\text{unph}}| = 1 + O(h) < 1; \quad |\lambda_{\text{ph}}| - |\lambda_{\text{unph}}| = O(h^2). \qquad (13b)$$

Consequently, the numerical noise (e.g., from the round-off error) has approximately the same magnitude as the "true" part of the numerical solution when one starts simulations from the zero initial condition. Therefore, to suppress this numerical noise, one needs to modify scheme (10), (11) so as to make

$$|\lambda_{\text{ph}}| - 1 > |\lambda_{\text{unph}}| - 1, \qquad (14a)$$

since this entails

$$|\lambda_{\text{ph}}|^n \gg |\lambda_{\text{unph}}|^n \qquad \text{for } n \gg 1. \qquad (14b)$$

We will accomplish this by modifying the BC (11), led by the following *key observation*. The unphysical modes will be attenuated in the entire grid if they are attenuated at the boundary. A way to attenuate a mode at the boundary is to lower its reflection coefficient, since then more of this mode would leak out. Therefore, the desired modification of (11) should meet two criteria:

(i) Attenuate the unphysical modes by lowering their effective reflection coefficient,

(ii) While not changing the reflection coefficient for the physical modes within the accuracy of the numerical scheme (i.e., $O(h)$ in this Section).

We will seek the modified version of BC (11) in the form:

$$E^+_0 + \theta^+_l \Delta_1 E^+_0 = R_l \left[E^-_0 + \theta^-_l \Delta_1 E^-_0 \right], \qquad (15a)$$

$$E^-_M - \theta^-_r \Delta_1 E^-_{M-1} = R_r \left[E^+_M - \theta^+_r \Delta_1 E^+_{M-1} \right], \qquad (15b)$$

where we have dropped the superscript 'n' in all $E^\pm$-terms, $\Delta_1 E_j \equiv E_{j+1} - E_j$, and $\theta^\pm_{l,r}$ are constants to be determined. To estimate the range of $\theta^\pm_{l,r}$ that could satisfy criteria (i) and (ii) above, let us start by considering unphysical modes (for criterion (i)) and the left boundary (the considerations for the right one are analogous). Substituting (12) with $\rho_{\text{unph}} \approx -1$ (from (13a)) into (15a), one finds:

$$E^+_{0,\,\text{unph}} \approx R_l \left(\frac{1 - 2\theta^-_l}{1 - 2\theta^+_l} \right) E^-_{0,\,\text{unph}} \equiv R_{l,\,\text{eff}} E^-_{0,\,\text{unph}}. \qquad (16)$$

The more rigorous analysis of Appendix C confirms that the effective reflection coefficient is indeed given by the above equation in the main order in h. For $\theta^+_l < 0$ and $\theta^-_l \sim 0.5$, one has $|R_{l,\,\text{eff}}| \ll |R_l|$, thereby leading to attenuation of the E^+-field at the left boundary compared to the case where the original BC (11) are used. This intuitive conclusion about diminishing reflection as $|R_{l,\,\text{eff}}|$ decreases to zero is also generally confirmed by the analysis; see the next subsection for a minor variation. Thus, criterion (i) is satisfied.

To see why criterion (ii) is satisfied, one uses similar calculations with $\rho_{\text{ph}} \approx 1$, obtaining from (15a):

$$E^+_{0,\,\text{ph}} + O(h) = R_l E^-_{0,\,\text{ph}} + O(h). \qquad (17)$$

These considerations also show that when the reflection coefficient is originally zero, then the modification of BC at the corresponding boundary along the lines of (15) is not expected to lead to attenuation of unphysical modes. Therefore, since we set $R_r = 0$ in this study, we do not vary $\theta_r^\pm$ in the results reported below.

Let us note that implementation of BC (15) in a code is straightforward and similar to (11). Namely, since E_1^+, $E_{0,1}^-$ and E_{M-1}^-, $E_{M,M-1}^+$ are determined by scheme (10) "in the bulk" of the grid, then E_0^+ and E_M^- are found from them by elementary algebra.

B. Numerical validation

Here we show that the above qualitative considerations for plausible ranges for $\theta_l^\pm$ are confirmed by direct simulations of system (10), (15), with simulations agreeing quantitatively with the analysis of Appendices B and C. The reader not interested in these technical details can skip to Section 3.

From Eqs. (43a), (49), and (48) it follows that the magnitude of a mode $\mathbf{E}(\rho)$ evolves as:

$$|\mathbf{E}(\rho)| \propto \exp\left[\text{Re}[\beta(\rho)]\, t\right], \tag{18}$$

where parameter $\beta(\rho)$ is defined in the first two of the aforementioned equations in Appendices B and C and can be found as explained there. Then the quantity

$$\Delta\gamma_{\text{anal}} \equiv \text{Re}[\beta]_{\text{ph}} - \text{Re}[\beta]_{\text{unph}} = \text{Re}[\beta(\rho=1)] - \text{Re}[\beta(\rho=-1)] \tag{19}$$

can be computed for any given pair (θ_l^+, θ_l^-) with the help of Eqs. (16), (17). The result is shown in Fig. 2(a). A positive value of $\Delta\gamma$ indicates that unphysical modes in the numerical solution are attenuated relative to the physical ones.

On the other hand, the rate of change of the exponent in (18) can be measured in simulations as follows. Upon multiplying the spatially non-periodic solutions of (10), (11) by a "window" function smoothly vanishing at $x = 0$ and $x = 1$ (e.g., by a super-Gaussian), one can take their Fourier transform. Given the correspondence between the mode parameter ρ and the wavenumber k, i.e. $\rho \sim \exp[ikx]$, one can then estimate $\text{Re}[\beta] \equiv \gamma$ in (18) as:

$$\gamma(k) = \frac{1}{t_2 - t_1} \ln \frac{|F[\mathbf{E}](k, t_2)|}{|F[\mathbf{E}](k, t_1)|}, \tag{20}$$

where $F[\ldots]$ stands for the Fourier transform. The counterpart of the analytical quantity (19), which determines how much unphysical modes are attenuated relative to the physical ones, is then

$$\Delta\gamma_{\text{numer}} = \gamma(k=0) - \gamma(k=\pi/h); \tag{21}$$

see the text after (13a). Figure 2(b) shows that the discrepancy between these analytical values and those found in simulations is indeed small.[1] From Fig. 2 one can also see that the region in the (θ_l^+, θ_l^-)-plane where $\Delta\gamma > 0$ is quite broad. Incidentally, it may be interesting to note that the maximum $\Delta\gamma$ occurs not at $\theta_l^- = 0.5$, where $R_{l,\text{eff}} = 0$, but slightly away from that point, which at the resolution of the Figure is at ($\theta_l^+ = 0.08$, $\theta_l^- = 0.42$). This may be related to the comment [11].

[1] except where $\Delta\gamma$ is strongly negative and hence of no practical interest
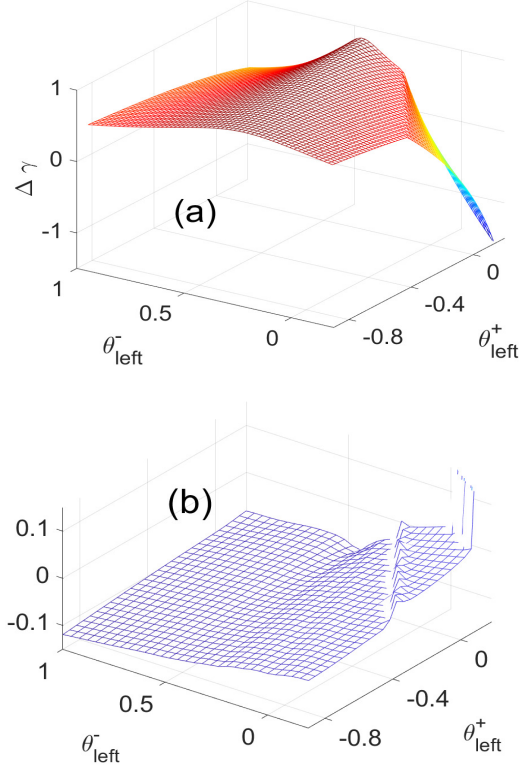

Fig. 2. (a): Analytical values of the quantity defined in (19). As noted in the text, positive values of $\Delta\gamma$ indicate that unphysical modes in the numerical solution are suppressed relative to the physical ones. (b): $\Delta\gamma_{\text{numer}} - \Delta\gamma_{\text{anal}}$. For each pair (θ_l^+, θ_l^-), the value $\Delta\gamma_{\text{numer}}$ was found as the mean of 100 simulations with different seeds of the random number generator of Eqs. (10), (15) (with $\theta_r^\pm = 0$), initial condition (6a), the equation parameters (8b) and $\kappa = 2$, and simulation parameters $h = 0.01$ and $t_{1,2}$ in (20) being 12.5 and 25. The standard deviation (not shown) was under 0.02 for all (θ_l^+, θ_l^-) except at the corner near $(0.2, -0.2)$.

As the final step in affirming the validity of our approach, in Fig. 3(a) we verify that the accuracy of the solution obtained with (10), (15) is indeed $O(h)$. Thus, a $O(h)$ change in the BC (see (17)) does not affect the overall $O(h)$ order of the scheme. However, one can see that having $\theta_l^\pm \neq 0$ does increase the magnitude of the error.

To ensure reproducibility of the numerical results, we will now describe how the errors in Fig. 3 were obtained. As noted at the end of Appendix A.2, one should distinguish between two kinds of numerical error: in the shape of the solution and in its time evolution constant β (that with the largest real part). For future reference, we present the exact solution of (9), (4) (with $E_{\text{inc}}^\pm \equiv 0$), which can be obtained from (44)–(46) (with $h \to 0$ in the last equation):

$$\begin{pmatrix} E_{\text{exact}}^+ \\ E_{\text{exact}}^- \end{pmatrix} = K(t) \begin{pmatrix} \beta \sinh[\alpha_+(x-1)] - \alpha_+ \cosh[\alpha_+(x-1)] \\ i\kappa \sinh[\alpha_+(x-1)] \end{pmatrix}, \tag{22a}$$

where α_+, β are computed as described in Appendix B,

$$K(t) \equiv 2c_+ \exp[\alpha_+ + \beta t], \tag{22b}$$

and c_+ is defined in (45). Then the two types of error are:

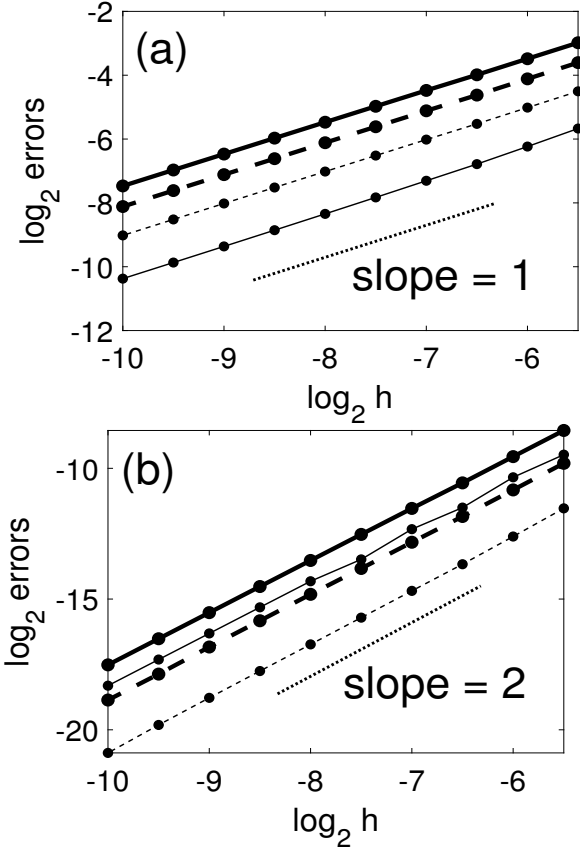$$\epsilon_\beta = |\beta_{\text{numer}} - \beta_{\text{exact}}|, \tag{23a}$$

Fig. 3. Numerical errors (23) versus step size. Panels (a) and (b) are for the first- and second-order schemes, respectively. The parameters of the simulations are described at the end of Section 2, and $t_{\max} = 30$. Thin lines: original BC (11); thick lines: $\theta_l^+ = 0$, $\theta_l^- = 0.4$ in (15) for (a) and $\eta^+ = 0$, $\eta^- = -0.2$ in (25) for (b). Solid and dashed lines show ϵ_{shape} and ϵ_β, respectively. The dotted line with the indicated value of slope is presented in each panel to facilitate visual comparison. The initial condition in all simulations was (24) with $s^\pm = O(1)$ (the exact value did not affect the results displayed). For simulations with the original BC (11), we set $D_\zeta^\pm = 0$, and for simulations with modified BC (15) and (25), we used $D_\zeta^\pm = 1$ (again, its exact value did not affect the results).

$$\epsilon_{\text{shape}} = \frac{1}{|K(t)|} \max_x \sum_{j=\{+,-\}} \sqrt{|E_{\text{numer}}^j(x,t) - E_{\text{exact}}^j(x,t)|^2},$$
(23b)

where β_{numer} is computed from the time evolution of $E_{\text{numer}}^-(0,t)$ similarly to Eq. (20) for $t_{1,2} \gg 1$. Since the constant c_+ could not be obtained from the initial condition in an efficient manner, we instead evaluated $K(t)$ as $E_{\text{numer}}^-(0,t)/(i\kappa \sinh[-\alpha_+])$, where $E_{\text{numer}}^-(0,t)$ is measured in the simulation. Note that it made sense to normalize the shape error by $|K(t)|$ since the latter quantity is proportional to the magnitude of the solution.

The initial condition for $E_{\text{numer}}^\pm$ was chosen as

$$E^\pm(x,0) = E_{\text{exact}}^\pm(x,0) + s^\pm \cdot (x-1) + \zeta^\pm(x), \quad (24)$$

with $K(0) = 1$, $s^+ = R_l s^-$, and $\zeta^\pm$ defined in (6); see caption to Fig. 3 for details. A nonzero $s^\pm$-term (satisfying the BC (4), (8b)) was used so as to suppress the high-frequency numerical artifact when using the original implementation (11) of the BC; see the discussion regarding Refs. [2], [4], [10] in Section 1. The parameters for the simulations were as listed in the caption to Fig. 2, except for the initial condition and the values of h.

III. EXTENSION TO THE SECOND-ORDER SCHEME

Here we illustrate how the above approach is extended to the second-order MoC scheme (32), (33) while continuing working with the reduced model (9). We replace the $O(h)$-accurate BC (15) with their $O(h^2)$-accurate counterpart:

$$E_0^+ + \eta_l^+ \, \Delta_2 E_1^+ = R_l \left[E_0^- + \eta_l^- \, \Delta_2 E_1^- \right], \quad (25a)$$

$$E_M^- + \eta_r^- \, \Delta_2 E_{M-1}^- = R_r \left[E_M^+ + \eta_r^+ \, \Delta_2 E_{M-1}^+ \right], \quad (25b)$$

where $\Delta_2 E_j \equiv E_{j-1} - 2E_j + E_{j+1}$. Using Taylor expansion of the smooth (i.e., physical) part of the numerical solutions $(E^\pm)_m^n$, one can show that these equations are the most general form of a second-order approximation to the exact BC (4) that uses variables at the latest time level. This observation addresses criterion (ii) listed before (15). To address criterion (i), one uses the reasoning found before Eq. (16) and obtains the effective reflection coefficient for the unphysical modes:

$$R_{l,\text{eff}} = R_l \left(\frac{1 + 4\eta_l^-}{1 + 4\eta_l^+} \right). \quad (26)$$

Then, similarly to the text found after (16), one predicts that the most efficient suppression of unphysical modes will occur around $\eta_l^- = -0.25$, as long as η_l^+ is far from -0.25. This prediction is confirmed by Fig. 4. We also verify, in Fig. 3(b), that the accuracy of the second-order scheme (32), (33) with the modified BC (25) is indeed $O(h^2)$. Similarly to the situation with the first-order scheme and modified BC, here also the magnitude of the error (but not its order in h) is greater for $\eta_l^\pm \neq 0$; however, the benefit of suppression of unphysical modes far outweighs the modest increase in the error. Also, since in the case that we consider here $R_r = 0$, then varying $\eta_r^\pm$ has practically no effect on the results.
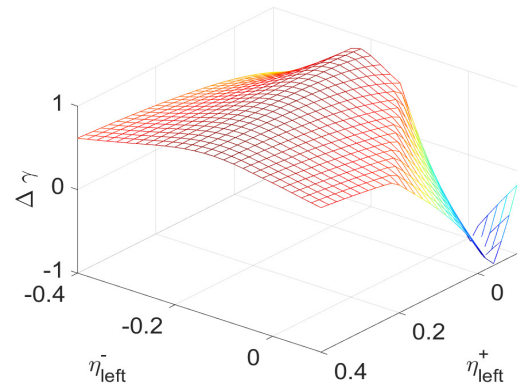

Fig. 4. Numerical values of the quantity defined in (21) found by the second-order scheme with modified BC (25). The simulations parameters are as described in the caption to Fig. 2. The standard deviation (not shown) was under 0.03 for all (η_l^+, η_l^-) except at the corner near $(-0.1, 0.1)$. Note three things when comparing this figure with Fig. 2(a). First, the shapes of the surfaces are very similar; second, the domain in this figure is about half that in Fig. 2(a) along each direction; third, the orientation of each of the horizontal axes in the two figures is opposite. The last two observations are consistent with the factors multiplying R_l in (26) and (16).

IV. Full model with the second-order scheme

We have verified that the modification of the BC described above eliminates the high-frequency artifact in the simplified model considered in Section 1; the solutions so obtained appear visually indistinguishable from those shown in Fig. 1(a). We now consider the full model (1)–(4) where we take dimensional parameters to be similar to those listed in [2]:

$$L = 400\,\mu\text{m}, \quad v_g = c/3.7, \quad N_0 = 1.5 \cdot 10^{18}\,\text{cm}^{-3}, \quad (27\text{a})$$

$$g = 10^{-16}\,\text{cm}^{-2}, \quad \Delta = 5, \quad \epsilon = 3 \cdot 10^{-17}\,\text{cm}^3,$$
$$\alpha_{\text{loss}} = 40\,\text{cm}^{-1}, \; \kappa = 40\,\text{cm}^{-1}, \; J = 5000\,\text{A/cm}^2, \; d = 0.2\,\mu\text{m},$$
$$\tau = 10\,\text{ns}, \quad B = 10^{-10}\,\text{cm}^3/\text{s}, \quad C = 3 \cdot 10^{-29}\,\text{cm}^6/\text{s};$$
$$(27\text{b})$$

also, the speed of light is $c = 3 \cdot 10^8$ m/s and the charge of electron is $q = 1.6 \cdot 10^{-19}$ A·s. The gain coefficient listed in (27b) corresponds to that in [2] where the confinement factor Γ is included. The BC in our simulations are given by (8b) (i.e., with a nonzero reflectivity of the left mirror), whereas in [2] the mirror reflectivities were zero, but there was a $\lambda/4$-phase shift in the middle of the medium. Using normalization (7a) and rounding to one or two significant figures, we obtain the following nondimensional values for parameters (27b):

$$g = 6, \quad \epsilon = 45, \quad \alpha_{\text{loss}} = 0.8, \quad \kappa = 1.6,$$
$$\frac{J}{qd} = 5 \cdot 10^{-3}, \quad \frac{1}{\tau} = 5 \cdot 10^{-4}, \quad B = \frac{1.5}{\tau}, \quad C = \frac{0.7}{\tau}. \quad (28)$$

We set $D_\zeta^\pm = 0$ in the initial condition (6) and consider two values for $D_\xi^+ = D_\xi^- \equiv D_\xi$ that result in a solution dominated by noise ($D_\xi = 5 \cdot 10^{-8}$) and one that is close to being visibly noise-free ($D_\xi = 5 \cdot 10^{-10}$). We simulate this model with the second-order scheme (32), (33) and the modified BC (25). The spontaneous emission (i.e., the noise terms) in (1) is simulated by Eqs. (37). To ameliorate the unphysically slow decay of the highest-frequency modes, we used $\eta_l^+ = 0$ and $\eta_l^- = -0.2$. Due to the reflection coefficient at the right boundary being zero, the BC there had the original form as in (11) (i.e., $\eta_r^\pm = 0$). The above values for $\eta_l^\pm$ may not have been optimal, but are still sufficient to perform the required task of suppressing the unphysical modes compared to the physical ones even in the presence of a significant amount of external noise, as it is apparent from Fig. 5(d). Let us note that even though the plots of the output power in both Figs. 1(c) and 5(c) appear "filled" (especially for the grey line in Fig. 5(c)), the reasons for that are different: In Fig. 1(c) the "filling" is due to the numerical artifact, while in Fig. 5(c) it is due to the physical noise.

V. Summary and extensions

We considered one aspect of the numerical solution of coupled-mode-type equations that describe dynamics of distributed-feedback semiconductor lasers, which have a partially reflecting mirror at (at least one of) the end points. The difficulty that such solution by, e.g., the method of characteristics (see below) faces is the artifact that the unphysical (i.e., highest-frequency) modes do not decay fast enough compared

to the physical (i.e., $O(1)$-frequency) modes, as the physics of the problem would dictate. Thereby, the numerical solution is significantly contaminated by noise,[2] even when the original physical problem does not include noise.

We demonstrated that this numerical artifact can be efficiently suppressed by modifying the numerical implementation of the boundary conditions (BC) at the partially reflecting end point(s) of the medium. The modified implementation, on one hand, preserves the original form of the BC for the physical modes; on the other, it can lower the reflection coefficient for the unphysical modes, thus facilitating their leakage out of the medium and hence causing them to decay faster than the physical modes. The technique proposed is not expected to be effective for gratings without reflective interfaces; however, such gratings are not usually considered for lasing, which is the context where the aforementioned artifact occurs. Let us also point out that the effectiveness of the modified BC technique does not depend on the grid spacing h.

We explained (see Appendix A.2) that it was essential to use a numerical scheme of deterministic order higher than one, even when the equations contain external noise, modeling which would typically lower the overall accuracy of the scheme. A scheme with second-order deterministic accuracy has been found to be adequate for this purpose. The modified form of the BC consistent with the second order of the scheme is given by Eqs. (25). We noted that the modification of the BC generally increases the numerical error by a factor of order two or sometimes higher. Therefore, if it is desired to minimize such an increase, an alternative to (25) could be used that has third-order accuracy:

$$E_0^+ + \mu_l^+ \, \Delta_3 E_1^+ = R_l \left[E_0^- + \mu_l^- \, \Delta_3 E_1^- \right], \quad (29\text{a})$$

$$E_M^- + \mu_r^- \, \Delta_3 E_{M-2}^- = R_r \left[E_M^+ + \mu_r^+ \, \Delta_3 E_{M-2}^+ \right], \quad (29\text{b})$$

where $\Delta_3 E_j = E_{j-1} - 3E_j + 3E_{j+1} - E_{j+2}$. Considerations similar to those found after (25) suggest that efficient suppression of unphysical modes will occur for $\mu_l^- \approx -1/8$ and $\mu_l^+ \geq 0$, and similarly at the right boundary.

Finally, let us point out two extensions of the results described above. First, we note that the idea of modifying BC in order to suppress reflection of the unphysical modes and thereby make them decay faster than physical ones, can be applied not only at the boundaries of the grating but also at any discontinuity, such as the $\lambda/4$-phase shift (see, e.g., [2], or [12] for a more recent reference). Below we discuss the first-order accurate modeling of this situation since a second-order numerical treatment of the condition satisfied at the $\lambda/4$-discontinuity is not available in the literature. The first-order accurate condition is found, e.g., in [13]:

$$(E^\pm)_{S\pm 1} = i\,(E^\pm)_S, \quad (30\text{a})$$

where the discontinuity is assumed to be at node $m = S$, and we have omitted the time index n. According to the method introduced in this work, a first-order accurate modification of this equation is, by analogy with (15):

$$E_{S+1}^+ + \sigma_a^+ \Delta_1 E_{S+1}^+ = i \left[E_S^+ + \sigma_b^+ \Delta_1 E_{S-1}^+ \right]; \quad (30\text{b})$$

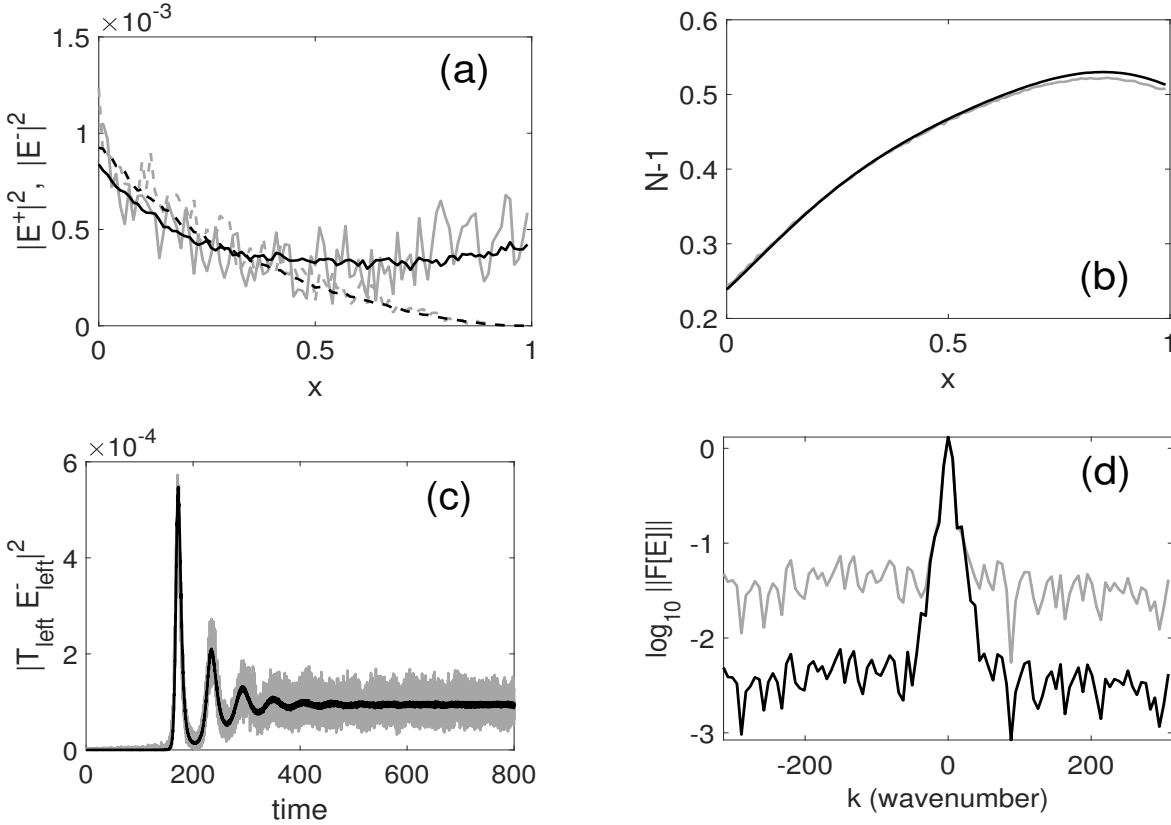[2]In the Introduction we hypothesized how this issue could be circumvented in earlier studies.

Fig. 5. Similar to panels (b)–(d) of Fig. 1, but obtained by the second-order scheme and modified BC (25) and *with* the external noise terms $\xi^\pm$. System parameters are listed in Section 4, and simulation parameters are $h = 0.01$ and $t = 800$ (corresponding to dimensional time of approximately 4 ns). Black and grey lines are for $D_\xi = 5 \cdot 10^{-10}$ and $5 \cdot 10^{-8}$, respectively. In panel (a), solid and dashed lines correspond to E^+ and E^-. In panel (d), $\|F[E]\| = \sqrt{|F[E^+]|^2 + |F[E^-]|^2}$.

and similarly for E^-; here $\sigma^+_{a,b}$ are constants similar to $\theta^+_{l,r}$. Following the logic of Section 2, the choice $(1 - 2\sigma^+_a) = -i\left(1 + 2\sigma^+_b\right)$ would preserve the pattern $E_m \propto (-1)^m$ across the node $m = S$ and thereby make that node (almost) transparent to the most rapidly oscillating, unphysical modes. If, in addition, one requires that $|\sigma^+_a|^2 + |\sigma^+_b|^2 = \min$ (since nonzero $\sigma^+_{a,b}$ moderately increase the numerical error; see Sections 2 and 3), then one finds:

$$\sigma^+_a = -(\sigma^+_b)^* = (1 + i)/4\,. \tag{30c}$$

In Fig. 6 we show the field and its spectrum obtained by solving Eqs. (1) by the first-order scheme (32), (34) with: $\xi^\pm \equiv 0$; the $\lambda/4$-discontinuity at $x = 0.5$ and the reflectivities of both left and right mirrors being 0 (as in [2]); and the rest of the parameters being the same as those used in Fig. 5 (i.e., also the same as in [2] except for κ). When the $\lambda/4$-discontinuity is modeled by (30a), one observes a strong high-frequency artifact in the simulated field and also its manifestation in the field's spectrum. On the other hand, when the $\lambda/4$-discontinuity is modeled by the modified condition (30b) with $\sigma^\pm_{a,b}$ being given by (30c), this numerical artifact is suppressed. Note that plotting power alone (as opposed to the field) may not reveal the artifact.

As the second extension, we note that the numerical artifact of slow decay of unphysical modes (before the modified BC are implemented) is not limited to the method of characteristics. For example, we have observed it when simulating

Eqs. (1)–(4) by both forms of the split-step method, considered in [14] and [15] and described in Appendix A.3. The mathematical reason for this is given in that Appendix. We also verified that the use of modified BC, such as (25), can efficiently suppress this high-frequency numerical artifact for the split-step method.

APPENDIX A
NUMERICAL SCHEME

A.1: Method of characteristics schemes

Using characteristics-based spatial variables $\chi^{(\pm)} = x \mp t$ (recall that $v_g = 1$ as per (7)) and the change of variables $(x,t) \rightarrow (\chi^{(\pm)}, t)$ in Eqs. (1a), while using the original variables in (1b), one rewrites system (1) as a set of pseudo-ODEs (ordinary differential equations):

$$\partial_t E^\pm = f^{(\pm)}(E^+, E^-, N) \quad \text{along } \chi^{(\pm)} = \text{const},$$
$$\partial_t N = f^{(N)}(E^+, E^-, N) \quad \text{along } x = \text{const}, \tag{31}$$

where we have included the noise terms into $f^{(\pm)}$. The numerical grid is: $x_m = mh$, $m = 0, 1, \ldots M$ and $t_n = nh$; any node $(x_m, t_n) \equiv (m, n)$ is an intersection point of some triplet of characteristics $\{\chi^{(+)} = \text{const}, \chi^{(-)} = \text{const}, \chi^{(N)} \equiv x = \text{const}\}$. Different variants of MoC schemes are obtained by using different ODE solvers along the characteristics. Below we present the scheme based on the explicit trapezoidal solver:

$$\overline{(E^\pm)}_m = (E^\pm)^n_{m\mp 1} + h\left(f^{(\pm)}\right)^n_{m\mp 1}, \tag{32a}$$
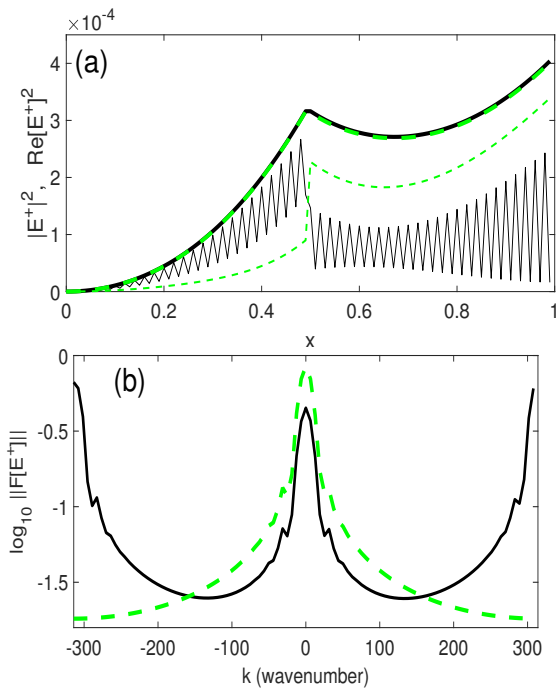
Fig. 6. Setup is described in main text after Eq. (30c). Simulation parameters h and $t_{\max}$ are the same as in Fig. 5. Results only for E^+ are shown; E^- is reflectionally symmetric to E^+ about $x = 0.5$. (a): Solid black and dashed green lines correspond to the discontinuity modeled by (30a) and by (30b) & (30c), respectively. Thick and thin lines correspond to power and squared real part. The powers almost coincide. (b): Fourier spectrum of the solution obtained with (30a) (solid black) and (30b) & (30c) (dashed green).

$$\overline{N}_m = N_m^n + h \left(f^{(N)} \right)_m^n ; \qquad (32b)$$

$$(E^\pm)_m^{n+1} = (E^\pm)_{m\mp1}^n + \frac{h}{2} \left[\left(f^{(\pm)} \right)_{m\mp1}^n + \overline{\left(f^{(\pm)} \right)}_m \right], \qquad (33a)$$

$$N_m^{n+1} = N_m^n + \frac{h}{2} \left[\left(f^{(N)} \right)_m^n + \overline{\left(f^{(N)} \right)}_m \right] ; \qquad (33b)$$

where

$$\left(f^{(\pm)} \right)_m^n \equiv f^{(\pm)} \left((E^+)_m^n, (E^-)_m^n, N_m^n \right),$$

$$\overline{\left(f^{(\pm)} \right)}_m \equiv f^{(\pm)} \left(\overline{(E^+)}_m, \overline{(E^-)}_m, \overline{N}_m \right),$$

etc. Note that if one lets

$$\overline{(E^\pm)}_m \equiv (E^\pm)_m^{n+1}, \qquad \overline{N}_m \equiv N_m^{n+1} \qquad (34)$$

in (32), then (32), (34) becomes a first-order accurate MoC scheme.

The implementation of BC (4) for the second-order scheme (32), (33) is:

$$\overline{(E^+)}_0 = T_l (E_{\text{inc}}^+)^{n+1} + R_l \overline{(E^-)}_0,$$
$$\overline{(E^-)}_M = T_r (E_{\text{inc}}^-)^{n+1} + R_r \overline{(E^+)}_M, \qquad (35a)$$

$$(E^+)_0^{n+1} = T_l (E_{\text{inc}}^+)^{n+1} + R_l (E^-)_0^{n+1},$$
$$(E^-)_M^{n+1} = T_r (E_{\text{inc}}^-)^{n+1} + R_r (E^+)_M^{n+1}. \qquad (35b)$$

When restricted to the first-order scheme (32), (34), the BC are given by (35a).

A.2: Modeling noise in Eqs. (1)

The following is based on two observations. First, modeling of noise with second-order accuracy in time is quite challenging (see, e.g., [16]); therefore, we model it here only with the half-order accuracy (i.e., the ensemble average of the numerical solution approaches the exact ensemble average as $O(h^{1/2})$). Second, the discrete version of the correlation relations (3) is given by:

$$\langle (\xi^\pm)_{m'}^{n'} (\xi^\pm)_m^n \rangle = 2D_\xi^\pm \frac{1}{h} \delta_{nn'} \frac{1}{h} \delta_{mm'}, \qquad (36)$$

where $\delta_{nn'}$ is the Kronecker delta and we have used the fact that the step size in both x and t equals h. Combining these observations, we model $\xi^\pm$ in (1a) by adding the noise term to the "corrector" equations (33a):

$$(E^\pm)_m^{n+1} = (\text{same as in (33a)}) + \sqrt{D_\xi^\pm} \left[(r_{\text{Re}}^\pm)_m^{n+1} + i (r_{\text{Im}}^\pm)_m^{n+1} \right], \qquad (37)$$

where $(r_{\text{Re, Im}}^\pm)_m^n$ are independent identically distributed normal variables with zero mean and variance one. The noise term in (1b) is modeled similarly, with the values for $(r^\pm)_m^{n+1}$ for the given n taken to be the same as in (37).

One can ask: Why use a numerical scheme whose deterministic order of accuracy (second) is higher than its stochastic order (half)? The justification for this has two aspects. First, the noise level in the device of interest is typically several orders of magnitude lower than the deterministic part of the solution (see Fig. 5). The second-order scheme (33) resolves that deterministic part, while the low-order treatment of the noise presented below accounts for the evolution of weak fluctuations on the background of the deterministic solution. Second, and more importantly, a first-order scheme has an $O(h)$-error not only in the shape of the solution (which most of the time would be acceptable), but also in the exponent governing the time evolution (i.e., the βt-term in (18) and (22b)); see also Fig. 3. Since one can easily have $t = O(1000)$ in simulations, an $O(h)$-error in β may significantly change the magnitude and phase of the solution (which we did, in fact, observe with the first-order scheme). Therefore, a $O(h^2)$, or higher-order, error in β is essential.

A.3: On two forms of a split-step method applied to Eqs. (1)

The authors of Ref. [14] proposed the following form of the split-step method to solve Eqs. (1a) for $E^\pm$ (without the $\xi^\pm$-terms). In the first substep, variables $E^\pm$ are advanced in time and space using only the first term (that in large parentheses) on the r.h.s. of (2a). In the second substep, according to [14], they need to be "evolved" *in space only* using only the ∂_x-terms on the l.h.s. of (1a) and only the κ-terms on the r.h.s. of (2a). We point out, however, that this second substep *as described in the previous sentence and in [14])*, cannot be implemented while respecting correct BC. The correct interpretation of this substep, which is able to respect the BC, should involve *both* partial derivatives on the l.h.s. of (1a).

The corresponding corrected formula is found in, e.g., Eq. (4) of [12]; in the notations introduced above it is:

$$\left(\begin{array}{c} E_{m+1}^+ \\ E_m^- \end{array} \right)^{n+1} = \exp[Gh] \cdot$$
$$\left(\begin{array}{cc} \mathrm{sech}(\kappa h) & i\,\tanh(\kappa h) \\ i\,\tanh(\kappa h) & \mathrm{sech}(\kappa h) \end{array} \right) \left(\begin{array}{c} E_m^+ \\ E_{m+1}^- \end{array} \right)^n ; \quad (38)$$

here G denotes the expression in the large parentheses in (2a).

A different form of the split-step method was described, e.g., in Sec. 2.4 of [15]. There, one of the substeps evolves the variables in (1a) using the full expression on the r.h.s. but disregards the ∂_x-terms on the l.h.s.. The other substep accounts for these omitted terms using the (exact) method of characteristics while setting the r.h.s. of (1a) to zero. One can straightforwardly show that the first-order accurate version of this form of the split-step method is given by the same Eq. (38) with sech and tanh being replaced by cos and sin. A second-order version of this method can be constructed as shown in [15], provided that the former substep is implemented with a second-order solver, such as the explicit trapezoidal solver.

It is easy to see that both these forms of the split-step method will exhibit the high-frequency numerical artifact whose suppression is addressed in this work. Setting $G = 0$ in (38) for the purpose of this argument and applying the von Neumann analysis to (38), one finds that the amplification factor λ for this scheme is:

$$\lambda = \mathrm{sech}(\kappa h) \cos(kh) \pm \sqrt{\mathrm{sech}^2(\kappa h) \cos^2(kh) - 1}, \quad (39)$$

and thus for all wavenumbers k, one has $|\lambda| = 1$. It was shown in [17] that non-periodic BC, such as (4), will modify $|\lambda| = 1$ for all k *away from* 0 *and* $k_{\max} = \pi/h$ (so that the solution's Fourier spectrum will look like that shown in Fig. 1(d)). However, they will leave $|\lambda(k \approx 0)| = |\lambda(k \approx k_{\max})|$ intact, which means that the unphysical, highest-frequency Fourier harmonics will evolve at the same rate as the physical ones with $k = O(1)$. The same considerations apply to the other form of the split-step method considered above.

Appendix B
Amplification factor $|\lambda|$ of physical modes of the numerical solution of Eqs. (9)

The main outcome of this Appendix will be justification of Eq. (18) for the evolution of the physical modes.

Substitution of (12) into (10) yields:

$$\left(\mathcal{C}^+ \rho^{-1} + \mathcal{C}^- \rho - \lambda I \right) \mathbf{u} = \mathbf{0}. \quad (40)$$

Our goal is to find ρ satisfying (13a) and then the corresponding λ. As an aside, let us note that an analogous analysis was performed in [17], but it *explicitly excluded* the modes satisfying (13a) because it had a different focus. In this Appendix, we limit ourselves to the physical modes, satisfying the first relation in (13a). Thus, let

$$\rho = 1 + \alpha h + O(h^2) \qquad \text{for some } \alpha = O(1). \quad (41)$$

In Appendix C we will handle the unphysical modes. Let us note that a more comprehensive and mathematically different analysis of Eqs. (9) with zero BC, leading to a counterpart of Eqs. (47) below, was first done in the classical paper [18].

The condition $\mathbf{u} \neq \mathbf{0}$ in (40) implies

$$\left(\rho^{-1} - \lambda \right) \left(\rho - \lambda \right) + h^2 \kappa^2 = 0. \quad (42)$$

For ρ given by (41), one verifies that λ must satisfy

$$\lambda = 1 + \beta h + O(h^2), \quad (43a)$$

where in the main order,

$$\alpha^2 = \beta^2 + \kappa^2. \quad (43b)$$

Recall that $|\lambda|$ is the amplification factor of the mode whose spatial profile is characterized by parameter ρ.

Thus, for a given value of β (or, equivalently, λ), there are two roots α satisfying (43b):

$$\alpha_\pm = \pm\sqrt{\beta^2 + \kappa^2}; \quad (43c)$$

note that $\alpha_\pm$ are, in general, complex. Also note that the subscript '$\pm$' in (43c) and below in this Appendix corresponds to the sign in that equation and is *in no way related to the superscript '$\pm$' in the main text*, which refers to forward- and backward-propagating fields. To each α (i.e., to each mode; see (41)) there corresponds an eigenvector $\mathbf{u}$:

$$\mathbf{u}_\pm = \left(\begin{array}{c} \beta - \alpha_\pm \\ i\kappa \end{array} \right); \quad (44)$$

the subscript of $\mathbf{u}$ has the same meaning as that in (43c).

Next, we substitute

$$\mathbf{E} = c_+ \mathbf{u}_+ + c_- \mathbf{u}_- \quad (45)$$

with yet undetermined constants $c_\pm$ into BC (15), where we make two simplifications. First, since (15) reduce to (11) up to $O(h)$ terms (see (17)), we will discard terms that are $O(h)$ relative to the main-order terms in all subsequent calculations. Thus, we can use the original BC (11) instead of (15a) in this Appendix. Second, for simplicity only, we set $R_r = 0$, consistently to the specific set of parameters (8b) that we use in this text for illustration of our theory. Thus, (45), (11), and (41) yield, in the main order:

$$\left(\begin{array}{cc} \beta - \alpha_+ - i\kappa R_l & \beta + \alpha_+ - i\kappa R_l \\ -i\kappa(1 + h\alpha_+)^M & -i\kappa(1 - h\alpha_+)^M \end{array} \right) \left(\begin{array}{c} c_1 \\ c_2 \end{array} \right) = \mathbf{0}, \quad (46)$$

where M is defined after (31). The condition that a nontrivial solution to (46) exists can be put into the form:

$$\beta = -\alpha_+ \coth \alpha_+ + i\kappa R_l, \quad (47a)$$

where we have used the approximation $(1 \pm h\alpha_+)^M \approx \exp[\pm\alpha_+(hM)] = \exp[\pm\alpha_+]$, the last equation being due to $hM = L = 1$ as per (7b). Equation (47a) can be used to find β once α_+ is known. To find an equation for the latter, one can square (47a) and use (43b) to eliminate β^2. After some algebra, the result is:

$$\alpha_+ = i\kappa \sinh \alpha_+ \left(R_l \cosh \alpha_+ \pm \sqrt{R_l^2 \sinh^2 \alpha_+ + 1} \right). \quad (47b)$$
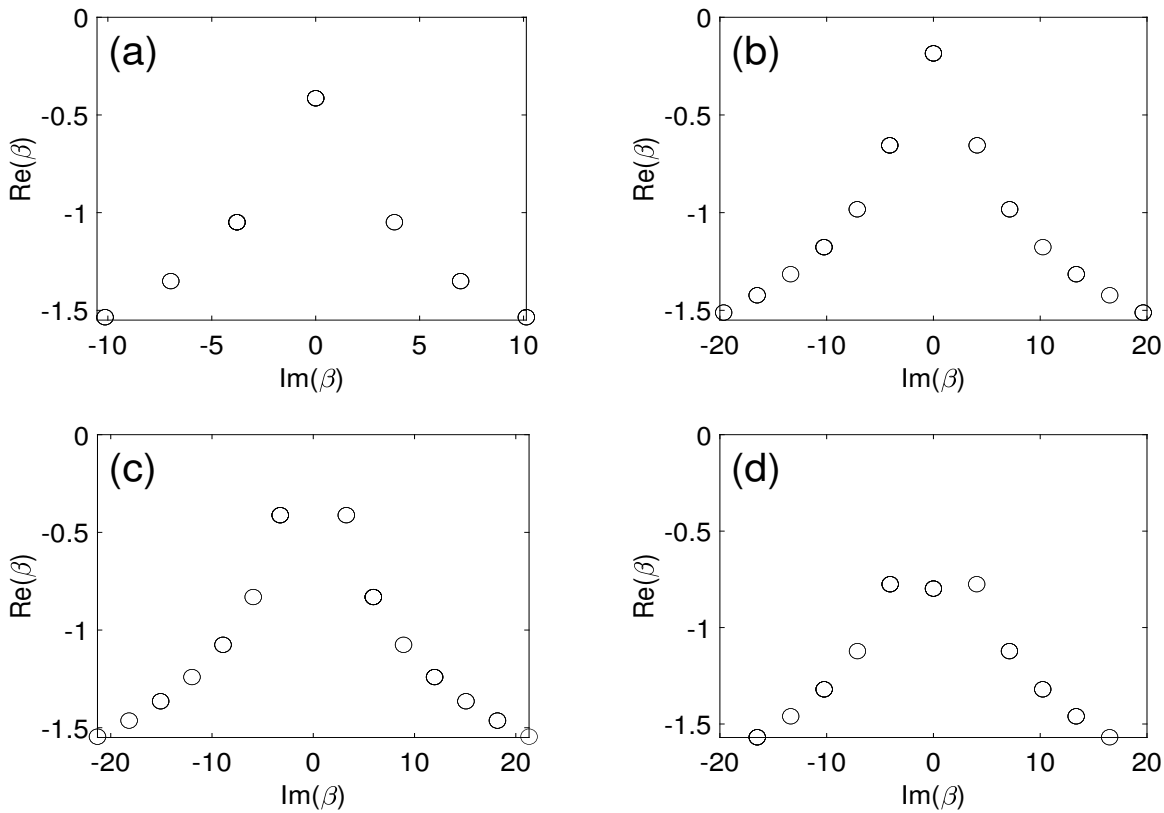
Fig. 7. Phase plot of β found as explained in the text. (a): $\kappa = 1$, $R_l = -i\sqrt{0.9}$; (b): $\kappa = 2$, $R_l = -i\sqrt{0.9}$; (c): $\kappa = 2$, $R_l = +i\sqrt{0.9}$; (d): $\kappa = 2$, $R_l = -i\sqrt{0.5}$.
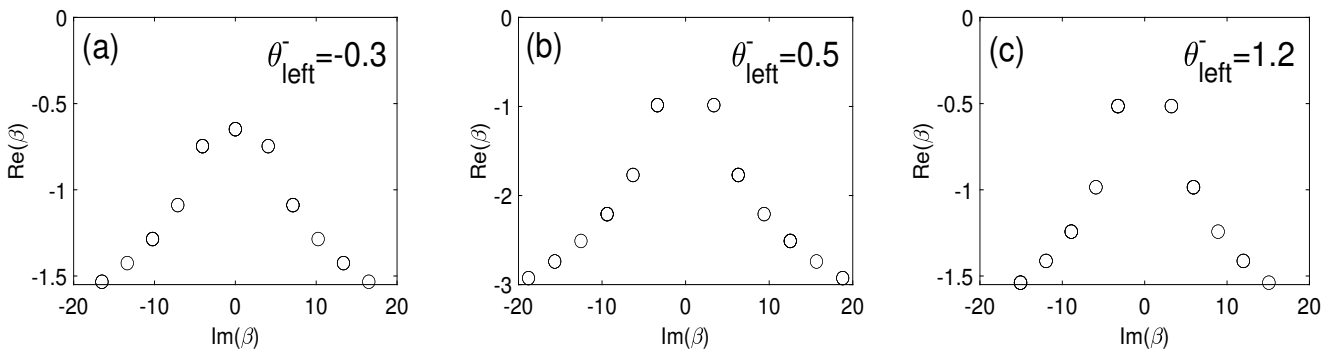

Fig. 8. Phase plots of β obtained as described in Appendix C for $\kappa = 2$, $R_l = -i\sqrt{0.9}$, $\theta_l^+ = -0.5$. The values of the only other parameter, θ_l^-, are shown in the panels. Note that the vertical scale in panel (b) is greater than that in (a) and (c) to emphasize a significant reduction of $\mathrm{Re}(\beta)$ occurring in this case.

Note that in the last equation, the '$\pm$' sign is *not* related to the superscripts and subscripts '$\pm$' used earlier; it simply indicates that α_+ can satisfy (47b) with *either* '$+$' or '$-$'. This equation, of course, agrees with that derived in [19] (see also [20]) for the more general case of $R_r \neq 0$. It can be solved numerically with, e.g., the Newton–Raphson method.

Thus, the time evolution of the physical modes, satisfying (41), is governed by the parameter β found from (47b) and (47a). Namely, via (43a) and the approximation

$$(1 + \beta h)^n \approx e^{\beta t}, \tag{48}$$

where $t = nh$, one finds that the mode amplitudes satisfy (18). Figure 7 shows the phase plots of β for some representative values of κ and R_l. In particular, in cases (a) and (b), the grating and the BC support a single main (longitudinal) mode,

while in cases (c) and (d) they support two such modes (with a third mode with $\mathrm{Im}\beta = 0$ in case (d) also playing a significant role in the dynamics for a very long time, since its $\mathrm{Re}\beta$ is smaller than that of the two main modes by a very small amount). The former design would correspond (if the system had gain) to the stable single-mode lasing regime observed in Fig. 5(c), while the latter design would show oscillating output power due to mode competition.

APPENDIX C
AMPLIFICATION FACTOR OF THE MOST UNPHYSICAL MODES OF THE NUMERICAL SOLUTION OF EQS. (9)

Here we follow the steps presented in Appendix B. All these steps up to and including Eq. (45) are repeated verbatim,

except that (41) and (43) are replaced, respectively, with

$$\rho = -(1 + \alpha h), \qquad \lambda = -(1 + \beta h), \qquad (49)$$

where we have omitted $O(h^2)$ terms. The minus sign above is consistent with that for ρ_{unph} in (13a).

To obtain the counterpart of (46), one needs to use Eqs. (15) (with $R_r = 0$, as before). The corresponding result is obtained straightforwardly but is quite cumbersome, and hence we do not display it. From that result, one derives, in the main order in h, the following counterpart of (47a):

$$\beta = -\alpha_+ \coth \alpha_+ + i\kappa R_{l,\,\text{eff}}, \qquad (50)$$

where $R_{l,\,\text{eff}}$ is defined in (16). Thus, quite intuitively, we have obtained the same result as if we had started with BC (11) where for the modes at hand (i.e., unphysical ones), the reflection coefficient is replaced with its main-order approximation [11]. Using (50) and (43b) one then finds that α_+ satisfies the same equation as (47a) with R_l being replaced with $R_{l,\,\text{eff}}$. Representative solutions for β obtained with that equation and (50) are plotted in Fig. 8. The time evolution of the modes' magnitude is given by relation (18), and hence the smaller values of $\text{Re}(\beta)$ correspond to greater suppression of unphysical modes relative to physical ones. Comparison of Figs. 8 and 7(b) shows that such a suppression can be expected for a large range of values θ_l^-. This expectation is confirmed by direct numerical simulations reported in Sections 2 and 3.

REFERENCES

[1] P. Vankwikelberge, G. Morthier, R. Baets, "CLADISS — A longitudinal multimode model for the analysis of the static, dynamic and stochastic behavior of diode lasers with distributed feedback," *IEEE J. Quantum Electron.*, vol. 26, pp. 1728–1741, 1990.

[2] L.M. Zhang, S.F. Yu, M.C. Nowell, D.D. Marcenac, J.E. Carroll, R.G.S. Plumb, "Dynamic analysis of radiation and side-mode suppression in a second-order DFB laser using time-domain large-signal traveling wave model," *IEEE J. Quantum Electron.*, vol. 30, pp. 1389–1395, 1994.

[3] L.A. Coldren, S.W. Corzine, M.L. Masanovic, *Diode Lasers and Photonic Integrated Circuits*, 2nd Ed. Hoboken, NJ: Wiley, 2012, Chaps. 5,6.

[4] A.J. Lowery, "Comparison between two recent large-signal dynamic DFB laser models," *IEE Proc.–J*, vol. 139, pp. 402–406, 1992.

[5] C.F. Tsang, D.D. Marcenac, J.E. Carroll, L.M. Zhang, "Comparison between 'power matrix model' and 'time domain model' in modelling large signal responses of DFB lasers," *IEE Proc.–Optoelectron.*, vol. 141, pp. 89–96, 1994.

[6] A.J. Lowery, "New dynamic model for multimode chirp in DFB semiconductor lasers," *IEE Proc.–J*, vol. 137, pp. 293–300, 1990.

[7] N.G.R. Broderick, C.M. de Sterke, K.R. Jackson, "Coupled mode equations with free carrier effects: a numerical solution," *Opt. Quant. Electron.*, vol. 26, pp. S219–S234, 1994.

[8] J. Chi, A. Fernandez, L. Chao, "Comprehensive modeling of wave propagation in photonic devices," *IET Commun.*, vol. 6, pp. 473–477, 2012.

[9] T.I. Lakoba, J.S. Jewell, "Higher-order Runge–Kutta-type schemes based on the Method of characteristics for hyperbolic equations with crossing straight-line characteristics," *Numer. Meth. PDEs*, https://doi.org/10.1002/num.22770.

[10] B.-S. Kim, J.-K. Kim, Y. Chung, S.-H. Kim, "Time-domain large-signal analysis of widely tunable DBR laser diodes with periodically sampled and chirped gratings," *IEEE Photon. Technol. Lett.*, vol. 10, pp. 39–41, 1998.

[11] Let us note that the derivation of (50) assumes that the omitted terms, which are, in fact, $O(h|\alpha_+|)$, are small compared to $|1 - 2\theta_{r,l}^\pm|$. This assumption is clearly violated in the case where $(1 - 2\theta_l^-) \approx 0$, which is most interesting for our purpose of reducing the effective reflection coefficient as per (16). Yet, the same derivation implies that in that case, $R_{l,\,\text{eff}}$ still has a small value, on the order of the omitted terms $O(h|\alpha_+|)$, and this leads to the same end result of having a smaller reflection coefficient for the unphysical modes.

[12] G. Zhao, J. Sun, Y. Xi, D. Gao, Q. Lu, W. Guo, "Design and simulation of two-section DFB lasers with short active-section lengths," *Opt. Express*, vol. 24, pp. 10590–10598, 2016.

[13] H.T. Hattori, V.M. Schneider, C.L. Barbosa, "Analysis of distributed-feedback lasers with fractionally organized gratings," *Appl. Opt.*, vol. 46, pp. 1283–1289, 2007.

[14] B.-S. Kim, Y. Chung, J.-S. Lee, "An efficient split-step time-domain dynamic modeling of DFB/DBR laser diodes," *IEEE J. Quantum Electron.*, vol. 36, pp. 787–794, 2000.

[15] T.I. Lakoba, "Numerical study of solitary wave stability in cubic nonlinear Dirac equations in 1D," *Phys. Lett. A*, vol. 382, pp. 300–308, 2018.

[16] P.E. Kloden, E. Platen, *Numerical Solution of Stochastic Differential Equations*. Berlin: Springer, 1992, Chap. 10 .

[17] T.I. Lakoba, Z. Deng, "Stability analysis of the numerical Method of characteristics applied to a class of energy-preserving hyperbolic systems. Part II: Nonreflecting boundary conditions," *J. Comput. Appl. Math.*, vol. 356, pp. 267–292, 2019.

[18] H. Kogelnik, C.V. Shank, "Coupled-wave theory of distributed feedback lasers," *J. Appl. Phys.*, vol. 43, pp. 2327–2335, 1972.

[19] W. Streifer, D.R. Scifres, R.D. Burnham, "Longitudinal modes in distributed feedback lasers with external reflectors," *J. Appl. Phys.*, vol. 46, pp. 247–249, 1975.

[20] H. Ghafouri–Shiraz, *Distributed Feedback Laser Diodes and Optical Tunable Filters*. Chichester, England: Wiley, 2003, Sec. 3.2.

Taras I. Lakoba received his M.S. degree in physics from Moscow State University in 1989 and Ph.D. degree in applied mathematics from Clarkson University in 1996.

He worked as a postdoctoral researcher at the University of Rochester and University of Central Florida, as well as a Member of Technical Staff at Bell Labs, Lucent Technologies, where he analyzed and simulated LambdaXtreme, an ultra-long-haul WDM transmission system. Since 2003, he has been with the Department of Mathematics and Statistics, University of Vermont, Burlington, VT, USA, where he is currently a Professor.

Prof. Lakoba's research interests include mathematical modeling of optical propagation in telecommunication fibers and photonic devices and development and analysis of numerical methods for nonlinear wave equations.

Benjamin L. Kotzen received a B.S. degree in mathematics from the University of Vermont in 2019.

Colin J. McKinstrie received a B.Sc. degree in mathematics and physics from the University of Glasgow, UK, in 1981 and a Ph.D. degree in plasma physics from the University of Rochester, USA, in 1986.

From 1985 to 1988, he was a Postdoctoral Fellow of Los Alamos National Laboratory, where he was associated with the Applied Physics Division and the Center for Nonlinear Studies. In 1988, he returned to the University of Rochester as a Professor of Mechanical Engineering and a Scientist in the Laboratory for Laser Energetics. While there, his main research interests were laser fusion and nonlinear fiber optics. From 2001 to 2014, he was a Member of the Technical Staff at Bell Laboratories, where his research concerned the amplification and transmission of optical pulses in communication systems, and applications of parametric devices in quantum information science. From 2014 to 2016, he continued this research at Applied Communication Sciences. In 2016 Dr. McKinstrie joined Futurewei Technologies, where he worked on semiconductor lasers, and in 2019 he joined CACI International, where he works on fiber lasers.